nature communications

Article

https://doi.org/10.1038/s41467-026-68719-3

Interfacial engineering via dipolar fullerene derivative for efficient tin halide perovskite indoor photovoltaics

Received: 25 June 2025

Accepted: 15 January 2026

Published online: 21 January 2026

Check for updates

Hongbin Xiao[1,2], Enhao Cui[1], Junfang Wang[1], Tianhua Liu[1], Xiaofang Wei[1], Junjie Huang[1], Muhammad Abdel-Shakour[1,3], Jie Li[4] ✉, Chunru Wang[4] ✉, Zonglong Zhu[5] & Xiangyue Meng[1] ✉

Modulating hot carrier dynamics is crucial in tin halide perovskite photovoltaics, particularly under indoor illumination with limited photon flux. Herein, a fullerene derivative bearing four piperazine groups (denoted as TPPC) is synthesized to engineer the perovskite/C_{60} interface. The TPPC molecule exhibits a dipole moment of 1.97 Debye, leading to enhanced adsorption energy on perovskite surface and robust interfacial interaction. The newly formed surface dipole optimizes the interfacial energy level alignment via a cascade gradient, enabling modulation of interfacial hot carrier dynamics. Consequently, TPPC-treated photovoltaic devices achieve a champion power conversion efficiency (PCE) of 22.49% and a maximum output power density (P_{out}) of 64.1 μW cm^{-2} under white light-emitting diode illumination (3000 K, 1000 lux, 285 μW cm^{-2}). Large-area (1.21 cm^2) devices attain a PCE of 17.94% (certified: 15.93%) and a maximum P_{out} of 51.2 μW cm^{-2} under the same illumination conditions.

Perovskite solar cells (PSCs) have attracted considerable attention owing to the exceptional characteristics of perovskite, including large adsorption coefficient, tunable bandgap, high charge carrier mobility, solution processibility, etc[1–5]. The power conversion efficiency (PCE) of multiple-junction PSCs has achieved 33.9% thus far[6], indicating great potential for commercial applications. Currently, owing to the emergency of a technology known as Internet of Things worldwide, it is imperative to fabricate indoor photovoltaic (IPV) devices to serve as power sources for electric appliances within a smart home system[7–11]. To date, the PCE of lead-based PSCs has reached 44.72% for IPV applications[12]. However, since the lead leakage is harmful to human health, especially for indoor applications, it is desirable to fabricate non-toxic and lead-free PSCs for IPV applications.

Reported lead-free PSCs targeting IPV applications are predominantly categorized into antimony (Sb)-based, bismuth (Bi)-based, and tin (Sn)-based devices[13–25]. Since tin and lead belong to the same group in the periodic table, tin halide perovskites share similar optoelectronic properties with their lead-based counterparts. This similarity has made them a promising alternative for IPV applications. Moreover, their bandgaps can be adjusted to exceed 1.65 eV through halide composition engineering to better match the indoor light spectrum and the theoretical photovoltaic efficiency limit can reach a remarkable 55%[26–28]. Therefore, tin halide perovskites exhibit great potential for IPV applications. Liao et al. first report the use of tin halide perovskites for IPV applications with a PCE of 10.45%[21]. They attribute such a low PCE to the oxidation of tin within perovskites. To solve this issue, they introduce catechin into tin halide perovskites as an

[1]Beijing Key Laboratory of Embodied Intelligence Computing, School of Optoelectronics, Center of Materials Science and Optoelectronics Engineering, University of Chinese Academy of Sciences, Beijing, China. [2]National Key Laboratory of Electronic Films and Integrated Devices, School of Integrated Circuit Science and Engineering, University of Electronic Science and Technology of China, Chengdu, China. [3]Chemistry Department, Faculty of Science, Assiut University, Assiut, Egypt. [4]Key Laboratory of Molecular Nanostructure and Nanotechnology, Beijing National Laboratory for Molecular Sciences, Institute of Chemistry, Chinese Academy of Sciences, Beijing, China. [5]Department of Chemistry, City University of Hong Kong, Kowloon, Hong Kong.
✉e-mail: lijie24@iccas.ac.cn; crwang@iccas.ac.cn; mengxiangyue@ucas.ac.cn

antioxidant. Ultimately, they achieve a maximum PCE approaching 12.81% and a maximum output power density (P_{out}) of 52.53 μW cm^{-2} under 1000 lux. The modification of hole-transport layer (HTL) is another effective strategy to increase the PCE of IPV devices. For example, Wang et al. demonstrate a PCE of 17.57% and a maximum P_{out} of 58.75 μW cm^{-2} for tin halide PSCs under the white light-emitting diode (WLED) illumination (2,956 K, 1062 lux, 334.41 μW cm^{-2}) by modifying poly(3,4-ethylene dioxythiophene) poly(styrene sulfonate) (PEDOT:PSS) with potassium thiocyanate (KSCN)[19]. They reveal that the KSCN interlayer not only optimizes the energy level alignment, but also improves the perovskite crystallization. To regulate the nucleation kinetics of tin halide perovskites, our group has previously incorporated cesium fluoride (CsF) into the PEDOT:PSS layer[29]. Results show that this method can enhance the adhesion of perovskites at the buried interface, thereby facilitating the heterogeneous nucleation. The CsF-incorporated PSCs demonstrate an efficiency of 20.12% and a maximum P_{out} of 57.32 μW cm^{-2} under the WLED illumination (3000 K, 1000 lux, 285 μW cm^{-2}).

As is well established, when a semiconductor is excited by incident photons with energies exceeding its band gap, hot carriers are generated[30–32]. Their excess energy is then dissipated through phonon emission until the carriers eventually relax to the bottom of the conduction band. This hot-carrier thermalization represents a major energy loss channel in photovoltaics, posing a fundamental limitation to the efficiency of PSCs as described by the Shockley–Queisser limit[33–35]. In principle, this limitation could be mitigated by extracting hot-carrier energy through the perovskite/electron transport layer (ETL) or perovskite/HTL interface prior to thermalization. Since low-light indoor illumination exhibits a substantially lower photon flux than one-sun illumination, the modulation of hot carrier dynamics is critically important to obtain the maximal photon utilization efficiency for IPV applications. It is noteworthy that the hot carrier cooling in tin halide perovskites typically takes place within nanosecond scale, which is significantly slower than that in conventional lead halide perovskites and silicon (within picosecond scale)[30,36–40]. Such a long cooling time provides a window of opportunity for efficient hot carrier extraction in tin halide perovskites. Effective modulations enable the extraction of high-energy hot carriers prior to their excess energy dissipation via lattice vibrations, thus improving the device performance. In the past few years, considerable progress has been attained in controlling hot carrier dynamics in perovskites, which mainly includes the use of quantum confinement effect in nanostructured perovskites[41,42], the incorporation of plasmonic nanoparticles into perovskite films[43,44], and the engineering of exciton-phonon coupling to slow down the hot carrier relaxation in perovskites[37,45]. However, the efficient extraction of hot carriers in perovskite photovoltaic device under low-light indoor illumination still remains a big challenge for IPV applications.

Herein, a multifunctional fullerene (C_{60}) derivative with four piperazine groups (denoted as TPPC) is synthesized and used to modulate hot carrier dynamics at the perovskite/C_{60} (PVK/C_{60}) interface. The TPPC molecule exhibits a dipole moment as high as 1.97 Debye, indicating its interaction with perovskite to form surface dipoles. This strong interaction is confirmed by the increased adsorption energy of TPPC on the perovskite surface, along with the distinct chemical shift observed in the ^{1}H nuclear magnetic resonance (^{1}H-NMR) spectrum after the incorporation of tin (II) iodide (SnI_2) into TPPC. The TPPC treatment also optimizes the interfacial energy level alignment by constructing a gradient, resulting in an extra back-surface electric field (E_{extra}). Since the E_{extra} is in the same direction as the built-in potential of the PVK/C_{60} interface, electron charge extraction at the interface is significantly improved. In addition, the TPPC-treated photovoltaic devices exhibit higher charge mobility, accelerated electron extraction and elevated charge collection efficiency. As a result, the modified IPV devices obtain a champion PCE of 22.49%. The certificated PCE for the large-area (1 cm^2) photovoltaic devices is as high as 15.93%. More importantly, the encapsulated devices exhibit enhanced operational stability, where ~91% of its initial efficiency is maintained after 2000 h of continuous maximum power point (MPP) tracking under simulated 1000 lux illuminance (ISOS-L-3 protocol) in ambient air (humidity: 40 ± 10%, temperature: 25 ± 5 °C). The strategy of modulating interfacial hot carrier dynamics with fullerene derivatives provides valuable guidance for improving the performance of IPV devices.

Results

Interaction between fullerene derivative and perovskite

The synthetic route for the TPPC molecule is illustrated in Fig. 1a. First, chlorofullerene ($C_{60}Cl_6$) was prepared by reacting C_{60} with excess iodine monochloride (ICl). Subsequently, tert-butoxycarbonyl (Boc) protected TPPC (TPPC-Boc) was produced by reacting $C_{60}Cl_6$ with piperazine in the presence of cumene hydroperoxide (CHP). Finally, TPPC molecules were obtained by replacing the Boc groups in TPPC-Boc with trifluoroacetic acid (TFA) in dichloromethane (CH_2Cl_2). Supplementary Figs. 1–4 depict the high-performance liquid chromatography (HPLC) analysis, electrospray ionization mass spectrometry mass spectra (ESI-MS), ^{1}H-NMR spectroscopy and ^{13}C-NMR spectroscopy of the prepared TPPC-Boc and TPPC molecules, respectively. These results demonstrated the successful syntheses of the fullerene derivatives with high purity. The electrostatic potential distribution of TPPC is shown in Fig. 1b. Obviously, the positive potential primarily localizes around the carbon (C) and hydrogen (H) atoms. While the negative potential concentrates around the nitrogen (N) atoms, suggesting the potential interaction with the positive Sn^{2+} of the tin halide perovskite. Furthermore, the TPPC molecule exhibits a dipole moment as high as 1.97 Debye, which further validates its interaction with perovskite to form the surface dipole.

To verify the potential interaction between TPPC and perovskite, density functional theory (DFT) calculations were performed. For comparison purposes, we first calculated the adsorption energy (E_{ads}) of C_{60} on the perovskite surface. As expected, the obtained E_{ads} was as low as −0.02 eV due to the weak physical interaction between C_{60} and perovskite (Fig. 1c). In contrast, the E_{ads} value (−1.06 eV) of TPPC on the perovskite surface was significantly increased compared to C_{60}, as depicted in Fig. 1d and Supplementary Fig. 5. It is noteworthy that the E_{ads} value of TPPC on the SnI_2-terminated perovskite surface (−1.06 eV) was significantly higher than that on the formamidinium bromide (FABr)-terminated surface (−0.18 eV). This suggested that TPPC molecules preferred to adsorb on the SnI_2-terminated perovskite surface due to the robust Lewis base-acid interaction between TPPC and SnI_2. Furthermore, the E_{ads} value (−0.21 eV) of C_{60} on the TPPC-treated perovskite was significantly higher than that on the untreated perovskite (−0.02 eV) because of the strong π-π interactions between fullerenes (Supplementary Fig. 6). This is advantageous for establishing an effective contact between perovskite and C_{60}, which facilitates electron transfer and prevents non-radiative recombination.

The Sn-N interaction could be validated by comparing the ^{1}H-NMR spectra of TPPC and TPPC+SnI_2. As depicted in Fig. 1e, the spectrum of TPPC exhibited a characteristic peak at the chemical shift of 9.02 ppm, while the peak showed a distinct shift of 0.22 ppm for TPPC+SnI_2. This pronounced shift clearly indicated a strong interaction between TPPC and SnI_2. Furthermore, the shift in the high-resolution X-ray photoelectron spectroscopy (XPS) spectrum of iodine (I) 3 *d* also confirmed the existence of this interaction (Fig. 1f). In addition, the TPPC molecule features four piperazine units in its skeleton, giving it strong basicity. This basicity effectively suppressed the oxidation of Sn^{2+} in the perovskite film. As revealed by the high-resolution XPS spectrum of Sn 3 *d* (Fig. 1g), the Sn^{2+} content in the perovskite film showed a notable rise from 63% to 76% upon the incorporation of TPPC.

The robust interaction between TPPC and perovskite could modulate the properties of perovskite films. According to the scanning

https://doi.org/10.1038/s41467-026-68719-3

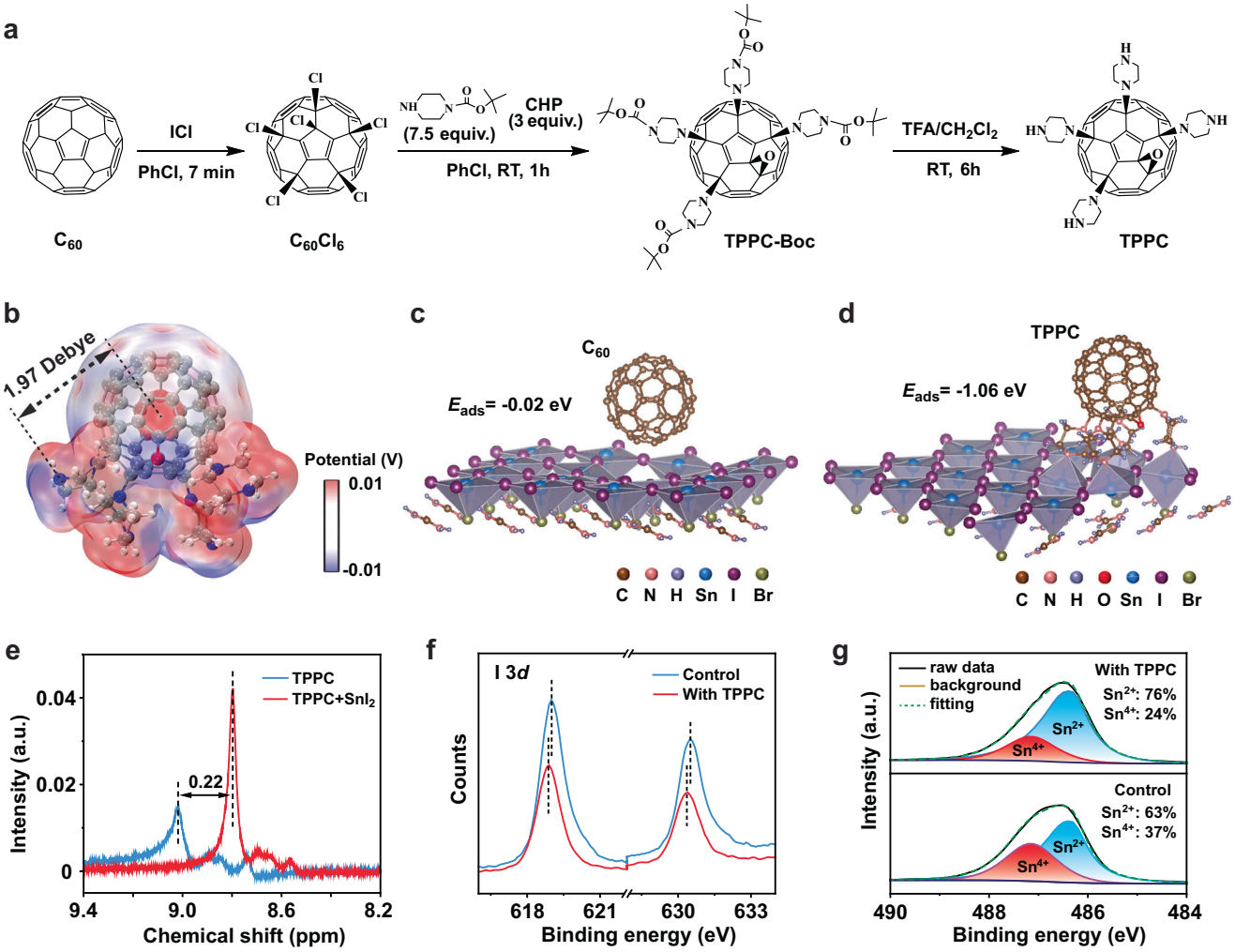

Fig. 1 | The synthetic route of TPPC and characterizations of the interaction between TPPC and perovskite. a Synthetic route of TPPC. **b** The electrostatic potential distribution and dipole moment of TPPC. The structural models and adsorption energies (E_{ads}) of C_{60} (**c**) and TPPC (**d**) on the perovskite surfaces. **e** ^{1}H-NMR spectra of TPPC and TPPC+SnI_2 dissolved in DMSO-d_6 solution. High-resolution XPS spectra of I 3 *d* (**f**) and Sn 3 *d* (**g**) for pristine and TPPC-treated perovskite films.

electron microscope (SEM) images (Supplementary Fig. 7), it was evident that the TPPC treatment with an optimal concentration (0.1 mg mL^{-1}) suppressed the pinhole formation, thereby enhancing the perovskite film quality. This was supported by the photoluminescence (PL) mapping (Supplementary Fig. 8), where the modified film exhibited a more uniform and stronger PL intensity distribution than the pristine film. Furthermore, the atomic force microscopy (AFM) images and their corresponding line-scan height profiles also suggested the formation of a smoother perovskite film subsequent to TPPC treatment (Supplementary Fig. 9). X-ray diffraction (XRD) patterns were also measured to examine the crystallinity variation of perovskite film after TPPC treatment. The improved crystallinity and enlarged grain size of the TPPC-treated perovskite film were evidenced by the stronger and sharper diffraction peaks at the (100) and (200) planes (Supplementary Fig.10). Specifically, the full width at half-maximum (FWHM) narrowed from 0.08° to 0.06° after TPPC treatment. According to the grazing-incidence wide-angle X-ray scattering (GIWAXS) patterns and the azimuthally integrated plots of the scattering vector (*q*)-dependent intensity (Supplementary Fig. 11), we could observe multiple well-defined diffraction peaks (e.g., (100), (011), (022), (211), (122), (120), and (208)), unequivocally confirming the formation of tin halide perovskite[5]. The GIWAXS patterns also validated the enhancement of the film crystallinity after TPPC treatment (Supplementary Fig. 11a,b), particularly as evidenced by the (100) diffraction plane. Additionally, according to the intensity-*q* plots (Supplementary Fig. 11c-h), the characteristic peaks showed no obvious shifts after TPPC treatment, demonstrating that the TPPC molecules did not incorporate into the lattice or alter the bulk crystal structure of perovskite. In summary, it can be concluded that the strong interaction between TPPC and the perovskite can suppress the oxidation of Sn^{2+}, leading to reduced defect density and enhanced film crystallinity. Consequently, the overall quality of the perovskite film is improved after TPPC treatment.

Optimization of the perovskite/fullerene interface

In order to demonstrate the optimization of the PVK/C_{60} interface, we examined the energy level alignment by analyzing the bandgap, work function (W_F), conduction band and valence band of pristine perovskite film, TPPC-modified perovskite film and C_{60} film. These parameters were determined from the Tauc plot of the ultraviolet-visible (UV-Vis) absorption spectrum (Supplementary Fig. 12) and ultraviolet photoelectron spectroscopy (UPS) (Supplementary Fig. 13). Severe charge carrier recombination was observed at the untreated PVK/C_{60} interface, as depicted in Supplementary Fig. 14. In contrast, an energy level gradient was established at the modified interface owing to the downward band bending of the TPPC-treated perovskite surface

https://doi.org/10.1038/s41467-026-68719-3

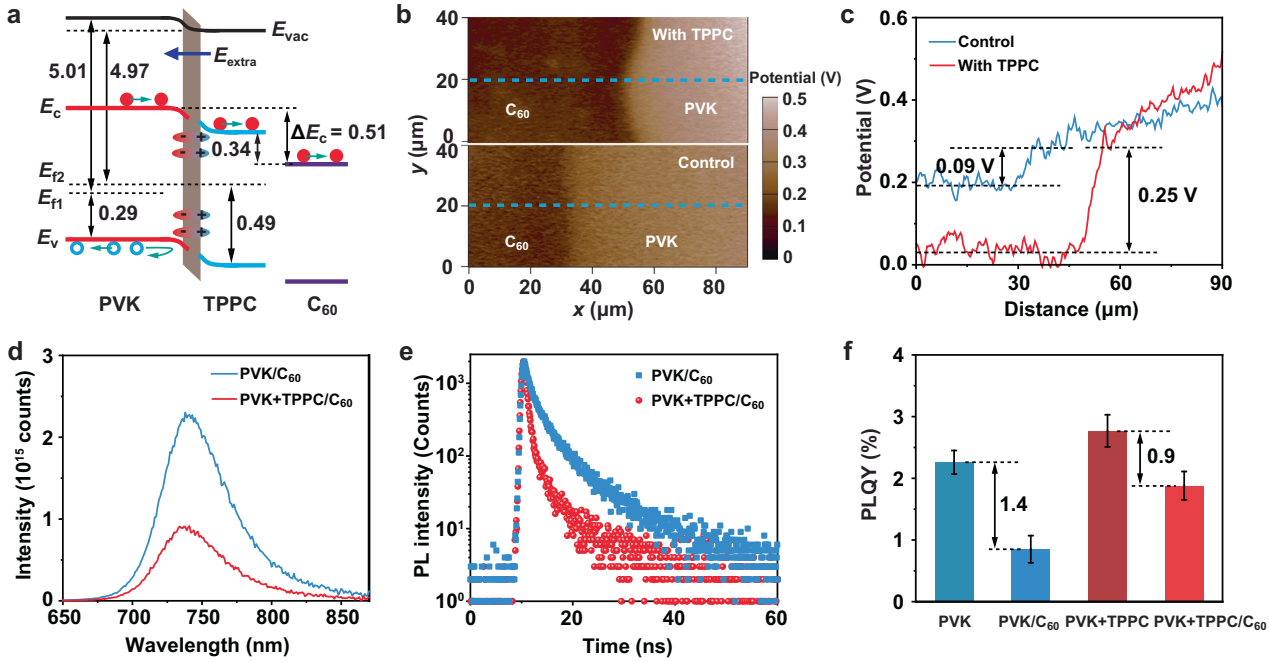

Fig. 2 | Energy level diagrams and optical properties for the PVK/C_{60} interface with and without TPPC treatment. a Energy level diagram of the PVK/C_{60} interface with TPPC treatment. E_{vac} represents the vacuum level energy, E_c represents the conduction band energy, E_v represents the valence band energy. E_{f1} and E_{f2} represent the fermi level energy of bulk perovskite and the TPPC-treated perovskite surface, respectively. **b** KPFM images. **c** Potential distribution profiles along the blue dashed lines shown in (**b**). **d** PL spectra. **e** Measured TRPL spectra under the 450 nm laser illumination (fluence: 12.74 nJ cm^{-2}, repetition rate: 1 MHz). **f** PLQYs for PVK, PVK/C_{60}, PVK + TPPC and PVK + TPPC/C_{60} layers under the Xenon lamp illumination (wavelength: 450 nm, power density: 2.27 mW cm^{-2}). The error bars show the standard deviations of 5 layers.

(Fig. 2a), which reduced the interfacial energy loss and suppressed interfacial charge carrier recombination by inhibiting the backflow of holes. It was noteworthy that the conduction band energy difference (ΔE_c) between perovskite and C_{60} decreased from 0.51 to 0.34 eV after TPPC treatment. Moreover, since the Fermi level (E_f) of the modified perovskite surface ($E_{f2} = -4.97$ eV) was higher than that of the bulk ($E_{f1} = -5.01$ eV), electrons would spontaneously flow from the perovskite surface to the bulk. This charge redistribution resulted in the formation of surface dipoles until the Fermi level alignment was reached. In such a case, the extra back-surface electric field E_{extra} pointing towards the substrate was established. Since the E_{extra} was in the same direction as the built-in potential of the PVK/C_{60} interface, electron charge extraction at the interface was significantly improved. The enhancement of the built-in electric field at the PVK/C_{60} interface could be further demonstrated by Kelvin probe force microscopy (KPFM) measurements (Fig. 2b). By analyzing the potential distribution along the blue dished line in KPFM images, it was observed that the potential difference of the TPPC-treated interface (0.25 V) was much larger than that of the untreated interface (0.09 V) (Fig. 2c), indicating an elevated electric field and agreeing well with the energy level analysis. To explore the reasons for the accelerated electron extraction at the modified interface, KPFM measurements were conducted to examine the impact of TPPC on the modulation of the work function of perovskite film. In contrast to pristine perovskite film, the TPPC-treated film exhibited a smaller contact potential difference (CPD, 0.65 *vs* 0.77 V) along a certain direction of the KPFM images (Supplementary Fig. 15), suggesting a reduced W_F owing to the formation of the surface dipole according to the following equation[46]

$$W_F = W_{tip} + e \times \mathrm{CPD} \quad (1)$$

where W_{tip} is the work function of the measuring probe and e is the unit charge, respectively. The modulation of work function was also confirmed through DFT calculations, where the calculated W_F of perovskite decreased from 4.87 eV to 4.41 eV after TPPC treatment (Supplementary Fig. 16). This decrease in W_F indicated a more *n*-type character of the perovskite surface, thereby facilitating electron extraction.

The optical properties of the PVK/C_{60} interface by TPPC treatment were also experimentally investigated. Compared with the pristine PVK/C_{60} film, the TPPC-treated film showed not only reduced PL intensity (Fig. 2d) but also a shorter lifetime in the time-resolved photoluminescence (TRPL) measurements (Fig. 2e), indicating the accelerated electron extraction at the modified interface. Additionally, the photoluminescence quantum yield (PLQY) of pristine perovskite film showed a decrease of 1.4% subsequent to the incorporation of C_{60} (Fig. 2f), indicating a substantial energy loss at the PVK/C_{60} interface. In contrast, the PLQY of the TPPC-treated perovskite film decreased by only 0.9% after the deposition of C_{60}, suggesting a reduced energy loss at the modified interface.

Modulations of interfacial hot carrier dynamics

The femtosecond transient absorption (fs-TA) spectrum was utilized to explore the influences of TPPC on the modulations of hot carrier dynamics at the PVK/C_{60} interface. It is well-known that the hot carrier cooling time is dependent on the phonon scattering rate under low and middle pump fluence, and the variation of cooling time can reflect the carrier extraction rate[37,47,48]. In the following, we first investigated the hot carrier dynamics under a low pump fluence of 1.05 μJ cm^{-2}. As depicted in the 2D pseudo-color images (Supplementary Fig. 17) and fs-TA spectra (Fig. 3a, b) within a short-time scale (1.2–81.9 ps), the photobleaching peaks occurred around 1.7 eV, due to the band edge filling effect. By normalizing the TA spectra near the band edge (Fig. 3c, d), the photobleaching signals were broadened in the high-energy region owing to the Fermi–Dirac statistics of hot carriers. To further investigate the decay dynamics of hot carriers, the high-energy tail (1.75–1.83 eV) of the spectrum was fitted using the Maxwell-Boltzmann distribution function as

https://doi.org/10.1038/s41467-026-68719-3

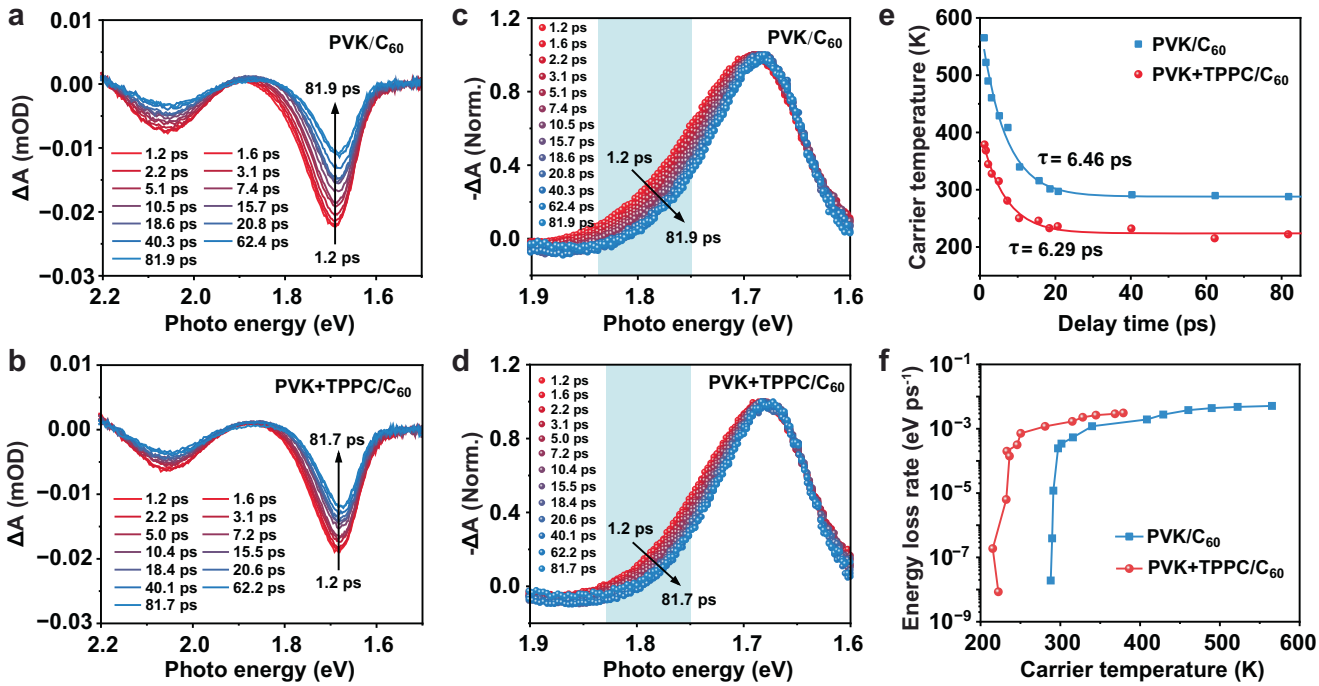

Fig. 3 | fs-TA analysis of the carrier dynamics at the TPPC-treated PVK/C_{60} interface under a pump fluence of 1.05 μJ cm^{-2}. fs-TA spectra of control (**a**) and TPPC-treated (**b**) PVK/C_{60} interfaces under different delay time. Normalized fs-TA spectra of control (**c**) and TPPC-treated (**d**) interfaces. **e** Variation of hot carrier temperature with delay time. τ represents hot carrier cooling time. **f** Dependence of the energy loss rate on the hot carrier temperature.

follows[46,49]

$$\Delta A(E) \propto e^{-(E-E_f)/k_B T_c} \quad (2)$$

where E is photo energy, k_B is Bolzman constant and T_c is hot carrier temperature, respectively. After extracting T_c from the fitting, the time-dependent carrier temperature was obtained (Fig. 3e). It was observed that the TPPC-treated PVK/C_{60} interface exhibited a shorter hot carrier cooling time (6.29 ps) than the untreated interface (6.46 ps). To further quantify the degree of error for the hot carrier cooling time, we made 4 samples without TPPC treatment and 4 samples with TPPC treatment. As shown in Supplementary Fig. 18, the hot carrier cooling time was 6.70 ± 0.19 ps and 6.00 ± 0.23 ps for the samples without and with TPPC treatment, respectively, suggesting that TPPC treatment could possibly facilitate hot carrier extractions at the interface and minimize thermalization losses of interfacial hot carriers. Note that we cannot definitely attribute the decrease in hot carrier cooling time to the accelerated hot carrier extraction at this stage, since a change in cold carrier extraction is another possibility. The final T_c value (224 K) of the treated interface was significantly lower than that of the untreated interface (288 K), indicating that the final formations of hot carriers in the modified perovskite exhibited a narrower Boltzmann distribution and a broader range of charge carrier extraction. In addition, the hot carrier energy loss rate (J_r) was calculated by the following equation[46,49]

$$J_r = -1.5 k_B dT_c/dt \quad (3)$$

As depicted in Fig. 3f, the TPPC-treated interface exhibited a higher energy loss rate than the original one, which also indicated the possibly accelerated hot carrier extraction at the modified interface. We also investigated the fs-TA spectra of the modified interface under a larger pump fluence of 2.63 μJ cm^{-2} (Supplementary Fig. 19). As shown in Supplementary Fig. 20, the TPPC-treated PVK/C_{60} interface showed a longer hot carrier cooling time (3.61 ± 0.32 ps) than the untreated interface (2.70 ± 0.35 ps). The prolonged hot carrier cooling time in the TPPC-treated interface at high fluence was probably ascribed to the reduction of defect density and suppression of Auger recombination and carrier-carrier scattering[33,50]. Compared to the hot carrier cooling time under the low pump fluence (1.05 μJ cm^{-2}), the shortening of hot carrier cooling time under high pump fluence (2.63 μJ cm^{-2}) primarily reflected the weakening of the hot phonon bottleneck effect and the intensification of recombination losses. In sum, we could draw the conclusion that owing to the suppressed Sn^{2+} oxidation, reduced trap density and optimized energy level alignment, the hot carrier extraction was possibly enhanced and the Auger recombination was efficiently mitigated at the TPPC-modified PVK/C_{60} interface.

Indoor photovoltaic performances

As TPPC treatment was able to accelerate hot carrier extraction at the PVK/C_{60} interface, TPPC-treated IPV devices were fabricated. Figure 4a shows a cross-sectional SEM image of the fabricated photovoltaic device, which consists of indium tin oxide (ITO)/PEDOT:PSS/PVK/C_{60}/bathocuproine (BCP)/silver (Ag). Supplementary Fig. 21 shows the schematic diagram of the experimental setup for evaluating the performance characteristics of IPV devices. Fig. 4b shows the current density-voltage (*J-V*) curves of the IPV devices based on pristine and TPPC-treated perovskite under the simulated indoor illumination (Supplementary Fig. 22, 3000 K, 1000 lux, 285 μW cm^{-2}). The *J-V* curves for devices treated with different concentrations of TPPC were also examined, as depicted in Supplementary Fig. 23. The control IPV devices exhibited a champion PCE of 15.19% with a maximum P_{out} of 43.3 μW cm^{-2} under the simulated indoor illumination, whereas the TPPC-treated devices achieved a remarkable champion PCE of 22.49% with an open circuit voltage (V_{oc}) of 0.72 V, a short-circuit current density (J_{sc}) of 140.0 μA cm^{-2}, a fill factor (*FF*) of 63.6% and a maximum P_{out} of 64.1 μW cm^{-2} (Supplementary Figs. 24,25, Supplementary Tables 1,2). Furthermore, we investigated the dependence of photovoltaic performances on incident light intensity and light color

https://doi.org/10.1038/s41467-026-68719-3

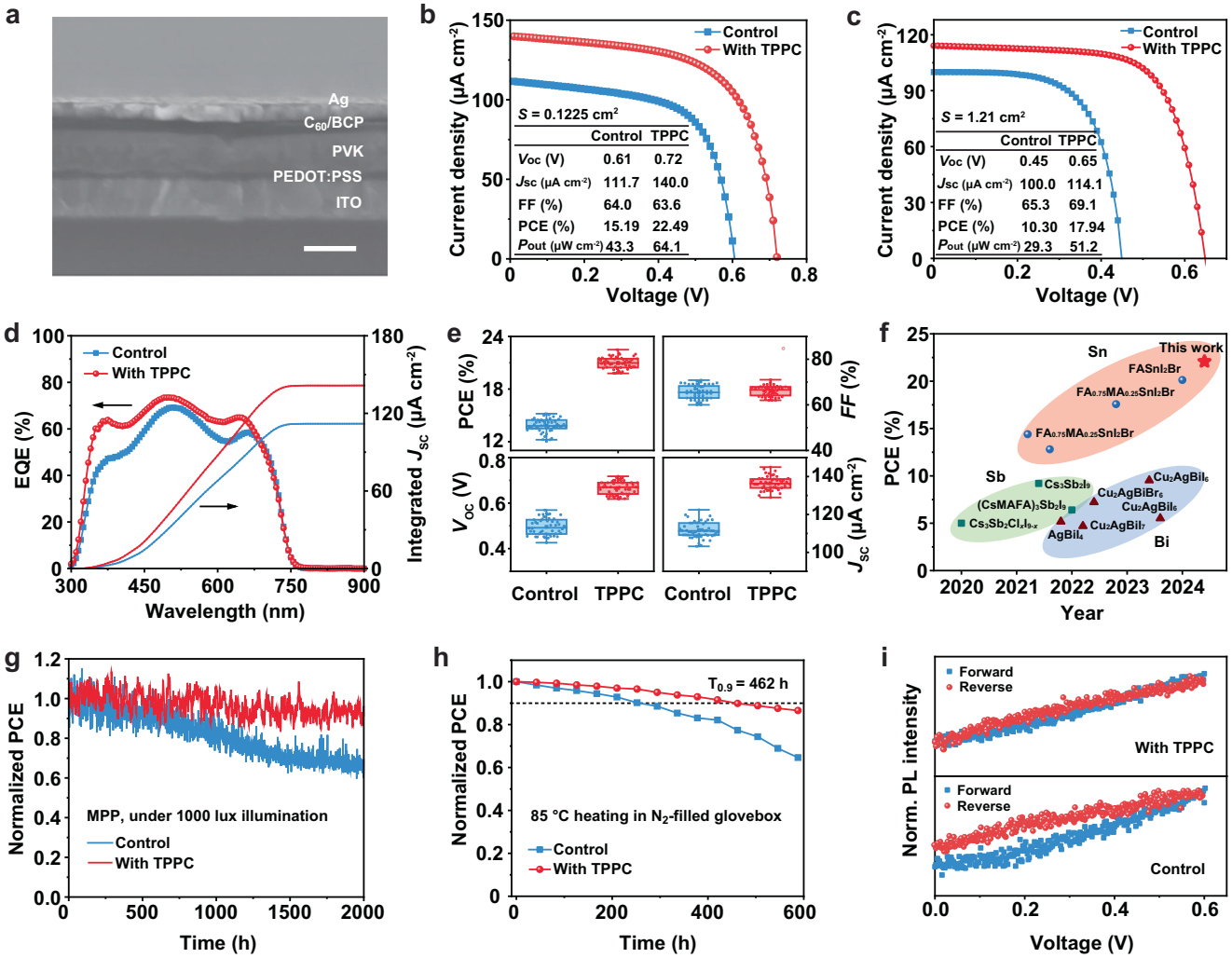

Fig. 4 | Performance characterizations of the control and TPPC-treated IPV devices. a Cross-sectional SEM image of the device. The scale bar is 200 nm. *J-V* curves of the devices with an effective area (*S*) of 0.1225 cm^2 (**b**) and 1.21 cm^2 (**c**) under WLED illumination (3000 K, 1000 lux, 285 μW cm^{-2}). **d** EQE and integrated J_{SC}. **e** Statistical photovoltaic parameters of PCE, *FF*, V_{oc} and J_{SC} for 51 devices under the WLED illumination (3000 K, 1000 lux, 285 μW cm^{-2}). For the box plots, the central line indicates the median, the box edges denote the lower and upper quartiles, the whiskers show the maximum and minimum values within 1.5 times the interquartile range, and the individual points represent outliers. **f** Development of PCE for lead-free perovskite-based IPV devices reported in literatures and this work to date. It should be noted that since all devices are measured under different light sources, we cannot make a 1:1 comparison across all data points, but this provides a general indication of progress. **g** Normalized PCE of the encapsulated IPV devices measured at maximum power point (MPP) under continuous 1000 lux light illumination (ISOS-L-3 protocol) in ambient air (humidity: 40 ± 10%, temperature: 25 ± 5 °C). **h** Thermal stability of encapsulated IPV devices annealed at 85 °C in N_2 atmosphere (ISOS-D-2 protocol). **i** In situ PL intensity under forward and reverse voltage scans of the devices.

temperature (Supplementary Figs. 26,27, Supplementary Tables 3,4). As expected, the PCE of the device increased with light intensity and reached the maximum under 3000 K. The IPV devices with a large effective area of 1.21 cm^2 were also fabricated. As depicted in Fig. 4c and Supplementary Table 5, the control devices with large effective areas obtained a champion PCE of 10.3% with a maximum P_{out} of 29.3 μW cm^{-2} under the simulated indoor illumination (Supplementary Fig. 22, 3000 K, 1000 lux, 285 μW cm^{-2}), while the TPPC-treated devices delivered a PCE as high as 17.94% with a maximum P_{out} of 51.2 μW cm^{-2}. Impressively, a certificated PCE of 15.93% was obtained for the TPPC-treated devices with an effective area of 1 cm^2 (Supplementary Fig. 28). It should be noted that since the severe shadow effect induced by the square mask (thickness: 200 μm) reduced the light intensity under the indoor light illumination, the certified PCE (15.93%) for the device with a mask is lower than that (17.94%) measured in our lab without masks. The integrated current densities calculated from external quantum efficiency (EQE) of the IPV devices were consistent with the measured *J-V* characteristics (Fig. 4d). It was noted that since the absorption of perovskite film did not show significant enhancement after TPPC treatment, the notable increase in J_{sc} of the TPPC-treated devices was attributed to the improvement of charge collection efficiency. For comparison purposes, we summarized the performance distributions of 51 control and TPPC-treated devices (Fig. 4e). The statistical analysis demonstrated excellent reproducibility of the IPV devices and significant enhancements in PCE, V_{OC} and J_{SC} due to the TPPC modification. Furthermore, based on the recent advancements in PCE of lead-free perovskite-based IPV devices (Fig. 4f, Supplementary Table 6)[13–19,21–25,31], it is evident that our measured PCE (22.49%) without a light mask is higher than that in the previous reports. The P_{out} of 64.1 μW cm^{-2} also ranks among the highest reported values thus far (Supplementary Table 6). It should be noted that since all devices reported in the literatures are measured under different light sources, we cannot make a 1:1 comparison across all data points, but this provides a general indication of progress. We should also note that the measurements without a mask may cause several issues, including inaccurate definition of the device's active area and

the inclusion of peripheral leakage currents. On the other side, since the severe shadow effect of the square mask (thickness: 200 μm) makes the active area of the device smaller than the mask's aperture area under the diffuse indoor illumination (Supplementary Fig. 29), the measured PCE with a mask is underestimated. Given the more pronounced impact of the shadow effect on the small-area devices, the photovoltaic performance of small-area devices was measured without a mask and not certificated, while that of large-area devices was certificated with a mask in this study.

Additionally, the stability of IPV devices was investigated according to the International Summit on Organic Photovoltaic Stability (ISOS) protocols[51]. The measured devices were encapsulated with the cover glass and UV-curing resin (Supplementary Fig. 30). The long-term operation stability was evaluated by MPP tracking under constant simulated 1000 lux light illumination (285 μW cm^{-2}, ISOS-L-3 protocol), as depicted in Fig. 4g. The TPPC-treated device maintained ~91% of its initial efficiency after 2000 h of continuous tests, whereas the pristine device retained only ~63% of the initial efficiency after the same duration. We also investigated the long-term operation stability of the devices by MPP tracking under constant simulated air mass 1.5 G illumination (100 mW cm^{-2}, ISOS-L-3 protocol), as shown in Supplementary Fig. 31. As expected, the TPPC-treated device preserved over 98% of its initial efficiency after 600 h of continuous tests (~60 °C), while the pristine device kept only 77% of the initial efficiency after the same duration. In the studies of the thermal stability of the IPV devices, it was found that the TPPC-treated device preserved 90% of the initial efficiency after 462 h ($T_{0.9}$) of thermal aging (85 °C) in nitrogen atmosphere (ISOS-D-2 protocol), surpassing the 252 h for the control device (Fig. 4h). The enhanced stability of the modified device primarily resulted from the reinforced PVK/C_{60} interface, which might suppress ion migration and perovskite degradation. To verify this, voltage-dependent PL intensity was investigated[52], as shown in Fig. 4i. In contrast to the control device, the TPPC-treated device presented a smaller PL-*V* hysteresis under the forward and revserse scans, indicating the mitigated ion migration. Water contact angle was also carried out to probe the TPPC-induced changes in the hydrophobicity of perovskite surface. As depicted in Supplementary Fig. 32, the water contact angle on the TPPC-treated perovskite film was much larger than that on the pristine one and it also showed a smaller variation with time. Therefore, the increased hydrophobicity of the modified perovskite film might be another reason for the improvement of the device stability.

To gain deeper insights into the modulation of charge carrier dynamics of the TPPC-treated IPV devices, we employed a series of complementary optoelectronic measurements, including photogenerated charge extraction by linearly increasing voltage (photo-CELIV), transient photocurrent (TPC) decay, intensity-modulated photocurrent spectroscopy (IMPS) and intensity-modulated photovoltage spectroscopy (IMVS). As the incident illumination scaled from 2% to 100%, the current density of the TPPC-treated device consistently exhibited a more rapid rise and reached its maximum much earlier than that of the control device (Fig. 5a, b). The charge mobility (μ) is determined by employing the following equation[53]

$$\mu = \frac{2d^2}{3At_{\max}^2(1+0.36\Delta j/j_0)} \tag{4}$$

where d is the film thickness, A is the voltage ramp rate, $t_{\max}$ is the time to reach the maximum current density, and j_0 and Δj are the initial current density and its variation, respectively. It was observed that the charge mobility of the TPPC-treated device was always higher than that of the control device (Fig. 5c). Since TPC allows to investigate the time-dependent extraction of charge carriers in solar cells, we further carried out TPC measurements to calculate the extracted charge carrier density (n_{CE}). From the TPC decay profiles under varied light intensity (Fig. 5d), it was observed that the TPPC-treated device showed a shorter TPC lifetime than the control device (Fig. 5e), indicating an accelerated charge extraction. This result matches well with the fs-TA analysis of hot carrier dynamics at the PVK/C_{60} interface. By further integrating the extracted current over time, we could obtain the extracted charge carrier density by the following equation[54–56]

$$n_{CE} = \frac{1}{SLq}\int_0^{t_e} j(t)dt \tag{5}$$

where S is the device area, L is the perovskite thickness, q is the unit charge, and t_e is the charge extraction time, respectively. As shown in Fig. 5f, the n_{CE} of the TPPC-treated device consistently outperformed that of the control device at varying light intensities. In addition, we employed IMPS and IMVS to probe the electron transport, recombination and charge collection dynamics in the IPV devices. As depicted in Fig. 5g, the electron transport time (τ_{tr}) of control and TPPC-treated devices was determined to be 1.3 and 0.9 μs, respectively, by using the following equation[57]

$$\tau_{tr} = \frac{1}{2\pi f_{IMPS}} \tag{6}$$

where f_{IMPS} is the peak frequency of the IMPS spectrum. The electron recombination time (τ_{rec}) of control and TPPC-treated devices under 10% light intensity was calculated to be 22.7 and 93.6 μs (Fig. 5h), respectively, by using the following equation[57]

$$\tau_{rec} = \frac{1}{2\pi f_{IMVS}} \tag{7}$$

where f_{IMVS} represents the peak frequency of the IMVS spectrum. Finally, under 10% light intensity, the charge collection efficiency (η_{cc}) was calculated to be 94.3% for the control device and 99.0% for the TPPC-treated device (Fig. 5i), according to the following equation[58]

$$\eta_{cc} = 1 - \frac{\tau_{tr}}{\tau_{rec}} \tag{8}$$

Therefore, the performance improvements in the TPPC-treated devices were attributed to the modulated carrier dynamics at the PVK/C_{60} interface, as evidenced by the enhanced charge mobility, improved charge extraction, and elevated charge collection efficiency.

In addition to modulating the carrier dynamics at the PVK/C_{60} interface, it was discovered that the TPPC treatment was capable of achieving surface passivation and suppressing nonradiative recombination of the IPV devices. As shown in Supplementary Fig. 33, the lower trap-filling limit voltage (V_{TFL}) observed in the electron-only device upon TPPC treatment indicated a reduced trap density in the modified perovskite film. This was validated by the trap energy-dependent trap density of state (tDOS) (Supplementary Fig. 34)[59], where the TPPC-treated device showed a lower tDOS within the trap energy range of 0.4–0.55 eV. Moreover, according to the dark *J-V* plots (Supplementary Fig. 35) and admittance spectra (Supplementary Fig. 36), the decreased dark current and capacitance both indicated that the modified perovskite film featured a lower defect density. The electrochemical impedance spectroscopy (EIS) was also measured under dark condition to analyze the nonradiative recombination in the devices. Supplementary Fig. 37 shows an increased recombination resistance after TPPC treatment, confirming the effective suppression of nonradiative recombination. The TPPC-treated device also showed an extended charge recombination lifetime according to the normalized transient photovoltage (TPV) decay profiles (Supplementary Fig. 38), which

https://doi.org/10.1038/s41467-026-68719-3

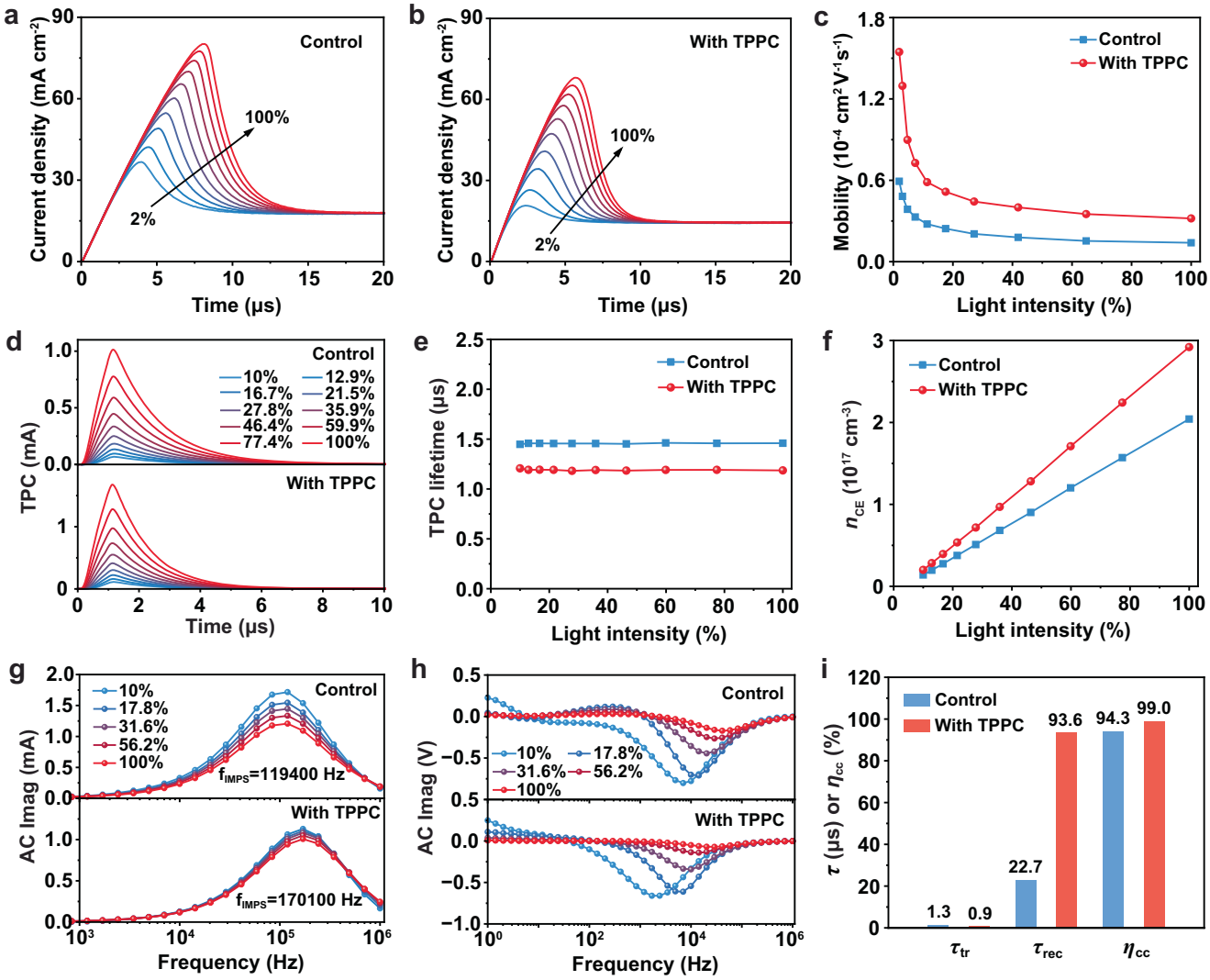

Fig. 5 | Modulations of carrier dynamics of the IPV devices by TPPC treatment. Photo-CELIV curves for control (**a**) and TPPC-treated (**b**) devices. **c** Light intensity-dependent mobility. **d** TPC decay profiles. **e** Relationship between TPC lifetime and light intensity. **f** Extracted charge carrier density (n_{CE}) as a function of light intensity. **g** IMPS spectra. f_{IMPS} represents the peak frequency. **h** IMVS spectra. **i** Statistics of carrier transport time (τ_{tr}), recombination time (τ_{rec}) and charge carrier collection efficiency (η_{cc}).

demonstrated a lower energy loss from charge recombination. Additionally, the built-in potential (V_{bi}) of the device was estimated by Mott–Schottky curves. As shown in Supplementary Fig. 39, the V_{bi} exhibited an increase from 0.66 V to 0.75 V after TPPC treatment. This improvement implied the enhancement of the inner electric field at the PVK/C_{60} interface, contributing to the prominently enhanced V_{OC} of the modified devices.

Discussion

By strategically modulating interfacial hot carrier dynamics through a fullerene derivative TPPC, this work unlocks the potential of tin halide perovskites for high-performance indoor photovoltaics. The TPPC molecule exhibits a dipole moment as high as 1.97 Debye, leading to increased adsorption energy on the perovskite surface than C_{60} and robust interfacial interaction. The formation of surface dipole helps to construct an energy level gradient at the modified PVK/C_{60} interface, resulting in elevated built-in potential. As a result, the TPPC-treated devices achieve a champion PCE of 22.49% and a maximum P_{out} of 64.1 μW cm^{-2} under the indoor illuminance of 1000 lux. The large-area (1.21 cm^2) devices deliver a record PCE of 17.94% (certified: 15.93%) and a maximum P_{out} of 51.2 μW cm^{-2}. Additionally, the encapsulated devices exhibit exceptional operational stability, where ~91% of their initial efficiency is maintained after 2000 h of MPP tracking under simulated 1000 lux light illumination. Meanwhile, the encapsulated devices retain 90% of their initial efficiency after 462 h of thermal aging (85 °C) in nitrogen atmosphere.

Methods

Materials

Unless otherwise noted, all chemicals were used in their as-received state, including tin (Sn) powder (99.8%, Sigma-Aldrich), iodine (I_2) powder (99.8%, Sigma-Aldrich), tin fluoride (SnF_2, 99%, Sigma-Aldrich), formamidinium bromide (FABr, 99.9%, TCI), 2-phenylethylamine hydrobromide (PEABr, 98%, aladdin), poly(3,4-ethylenedioxythiophene)-poly(styrenesulfonate) (PEDOT:PSS) (Mn=15,000–25,000, Xi'an P-OLED Co. Ltd.), fullerene (C_{60}, 99.9%, Sigma-Aldrich), bathocuproine (BCP, 99%, TCI), dimethyl sulfoxide (DMSO, anhydrous, >99.9%, Sigma-Aldrich), chlorobenzene (anhydrous, 99.8%, Sigma-Aldrich), and indium tin oxides (ITO) (Advanced Eletion Technology Co. Ltd.).

Synthesis of tin iodide solution

The SnI_2 solution was synthesized by the reaction of Sn and I_2 in DMSO. First, 0.85 mmol I_2 powder was dissolved in 1 mL DMSO. Subsequently, an excess of Sn powder (0.92 mmol) was added to the I_2 solution. Finally, the mixture solution was stirred overnight in a glovebox to obtain the SnI_2 solution.

Synthesis of fullerene derivative

First, $C_{60}Cl_6$ was prepared by reacting C_{60} with sufficient ICl. Following this, $C_{60}Cl_6$ was reacted with 7.5 folds of 4-(tert-butoxycarbonylaminoethyl)piperidine and 3 folds of 80% CHP in toluene for 1 hour. The crude product was first washed with a saturated aqueous solution of NH_4Cl and $NaHCO_3$, and then purified on a silica gel chromatography column with a toluene–ethyl acetate combination to obtain the solid TPPC-Boc (purity >98%). Lastly, TPPC (purity >97%) was prepared by eliminating the Boc groups with 10% TFA in CH_2Cl_2 for 6 h at room temperature.

Preparation of tin halide perovskite films

The precursor for the tin halide perovskite ($FASnI_2Br$) film was obtained by mixing 0.12 mmol PEABr, 0.68 mmol FABr and 0.12 mmol SnF_2 in 1 mL SnI_2 solution (0.8 M). The mixture solution was then subjected to magnetic stirring at 50 °C over a period of 3 h. Following this, the precursor solution was filtered with 0.22 μm polytetrafluoroethylene filters. After that, the perovskite precursor was deposited onto the ITO substrate by spin-coating (2000 rpm for 12 s, 5000 rpm for 60 s). At the 40_{th} second after the speed attained 5000 rpm, 135 μL of chlorobenzene was dispensed onto the substrate. Finally, the perovskite film was annealed at 70 °C for 30 min. For TPPC-treated perovskite film, 100 μL of TPPC dissolved in 2,2,2-Trifluoroethanol was deposited on the perovskite film via spin-coating at 5000 rpm for 30 seconds.

Fabrication of perovskite solar cells

First, a sequential cleaning protocol was applied to the patterned ITO glass substrates, comprising 15-minute ultrasonic treatments in detergent, deionized water, acetone, and ethanol. Then, the substrates were subjected to a 20-minute ultraviolet ozone treatment. After that, 200 μL of PEDOT:PSS solution was deposited onto the ITO substrate via spin-coating (4000 rpm, 30 s), followed by annealing at 150 °C for 20 minutes. Following this, the ITO substrates were placed into the glove box and the tin halide perovskite films were fabricated by the above method. Subsequently, 50 nm C_{60} layer and 5 nm BCP layer were deposited on the substrate via successive thermal evaporation. Finally, the Ag electrode (70 nm) was thermally evaporated through a mask (area: 0.1225 cm^2). To eliminate the pronounced shadow effect introduced by masks under indoor illumination, the performances of the small-area (0.1225 cm^2) devices were measured without masks. For the stability test, the devices were encapsulated with the cover glass (23 × 11.5 mm^2, internal rectangular groove: 19 × 7.5 mm^2) and UV curing resin (Lot NO. A20J01, 3014, ThreeBond). Specifically, a uniform layer of UV-curing resin was first applied to the cover glass. The cover glass was then immediately positioned onto the device. Subsequently, the device was placed in the chamber of the UV-curing lamp and exposed to UV light for 40 s. Finally, the device was transferred to a transition chamber and subjected to vacuum for 1 minute, resulting in a well-sealed encapsulated device.

Characterization

The purity of material was tested by HPLC (LC2030C 3D, Shimadzu). ESI-MS was measured using a mass spectrometer (Orbitrap Fusion LUMOs, Thermo Scientific). UV-Vis absorption spectra were recorded with a spectrophotometer (V-JASCO). PL, PLQY and TRPL measurements were carried out on an FLS1000 spectrometer. PL mappings were acquired by using the Raman image-scanning electron microscope. The film morphologies and cross-sections of the devices were characterized by SEM (JSM-6500F). XRD patterns were measured with a Rigaku SmartLab X-ray diffractometer (Cu Kα, λ = 1.54050 Å). ^{1}H-NMR spectra were acquired on a JEOL JNMECZ500R spectrometer (500 MHz). XPS measurements were conducted on a Thermo Scientific ESCALAB 250Xi spectrometer. FTIR spectra were acquired using a Thermo Scientific NICOLET iS50 spectrometer. GIWAXS data were collected at the 1W1A station of Beijing Synchrotron Radiation Facility. KPFM tests were conducted on a Bruker Bio-FastScan atomic force microscope. Contact angle tests were conducted using an Attension Theta Optical Tensiometer (Biolin Scientific, Sweden).

Femtosecond transient absorption spectrum

The fs-TA spectrometer consisted of an amplified Ti:sapphire laser system (central wavelength: 800 nm, pulse width: 25 fs, pulse repetition rate: 1 kHz, maximum pulse energy: 4 mJ) integrated with a Helios pump–probe system. The 800 nm fundamental beam was split into two paths. The majority was directed into an optical parametric amplifier to generate the 840 nm pump light, modulated by a 500 Hz mechanical chopper. A minor portion passed through a motorized delay line before being focused onto a sapphire to produce broadband probe pulses (430–820 nm or 800–1400 nm). The delay line controlled the optical path difference between the pump and probe lights for time-resolved measurements. Pump and probe beams were spatially and temporally overlapped on the sample.

Device measurements

The performances of the fabricated IPV devices were measured with an indoor light simulator (WLED, model: ILS-30) and a Keithley 2400 source meter. To evaluate the uniformity (U) of the light source, we mapped the spatial distribution of measured light power (P) across the sample stage using a power meter. Measurements were taken across a grid with 1 cm spacing. The irradiation uniformity was calculated by

$$U = 1 - \frac{P_{max} - P_{min}}{P_{max} + P_{min}} \times 100\% \quad (9)$$

where P_{max} is the maximum power, and P_{min} is the minimum power. Results showed that the WLED used in our experimental setup achieved a high uniformity of 98.1% over a 5 × 5 cm^2 area (Supplementary Fig. 40), confirming excellent irradiation homogeneity. To further evaluate the temporal stability (S) of the light source, we monitored the irradiance (I) of the WLED at its operating intensity for over 1 hour using the spectrometer. The value of S was then calculated by

$$S = 1 - \frac{I_{max} - I_{min}}{I_{max} + I_{min}} \times 100\% \quad (10)$$

where I_{max} represents the maximum irradiance, and I_{min} represents the minimum irradiance. As a result, the light source demonstrated excellent stability (Supplementary Fig. 41), with a S of 99.5% over the measurement period. During the J-V measurements, a consistent light source-to-substrate distance was maintained: 34.2 cm in our lab and 40.5 cm in the certification laboratory. These distances were chosen to ensure a sufficiently large and uniform illumination area. The spectrometer (Model: HS-IL) used in our IPV measurement setup has a cosine corrector. The purpose of using a cosine corrector on the spectrometer is to ensure the instrument accurately measures light incident from all angles, providing a response that is proportional to the cosine of the angle of incidence. This achieves accurate measurements of diffuse or oblique light. But it should be noted that while a cosine corrector was used for the spectrometer, a slight difference in the angular response between the spectrometer and the photovoltaic

device could still persist, representing a potential source of error in the measured irradiance and consequent current density. The used spectrometer has been calibrated by the manufacturer using a NIST-traceable standard light source prior to this study (Supplementary Fig. 42). EQE spectra were acquired with a QE-R3011 system. The measurements of TPC, TPV, capacitance-frequency spectra, Mott-Schottky plots, photo-CELIV, IMPS and IMVS were all performed using a Paios 4.1 instrument. The space-charge-limited current was characterized using a Keithley 2400 source meter to obtain the dark-state *J-V* curves. For all in-lab measurements, the light source, the device under test (DUT), and the spectrometer were all arranged in a normal incidence (0°) configuration. The active layer of the DUT and the detector of the spectrometer were placed parallel to the light-emitting surface of the light source. The measurements at the certification laboratory (FUJIAN METROLOGY INSTITUTE) were performed following their standard procedures, and a normal incidence geometry was also employed.

Density functional theory calculations

The electrostatic potential profiles, molecular dipole moment and geometry of TPPC were calculated using Gaussian 09 at the B3LYP/6-31 G* level. All DFT calculations were performed using the Vienna Ab initio Simulation Package. The generalized gradient approximation of Perdew–Burke–Ernzerhof was adopted for the exchange–correlation potential. The projector augmented-wave method was used to describe the ion core/valence electron interactions. A plane-wave cutoff energy of 450 eV was employed. The models were geometrically optimized until the Hellmann–Feynman forces were less than 0.02 eV/Å and the energy change was below 10^{-5} eV. For the adsorption models, the DFT-D3 correction was employed for the dispersion interactions across all atoms. The adsorption energy of an additive molecule on the perovskite surface was calculated by

$$E_{ads} = E_{pero+addi} - E_{pero} - E_{addi} \quad (11)$$

where $E_{pero+addi}$, E_{pero} and E_{addi} denote the energies of the passivated perovskite, pristine perovskite and additive molecule, respectively.

Reporting summary

Further information on research design is available in the Nature Portfolio Reporting Summary linked to this article.

Data availability

The data that support the findings of this study are included in the article and its Supplementary Information. Any additional information can be obtained from corresponding authors upon request. Source data are provided with this paper.

References

1. Liu, S. et al. Buried interface molecular hybrid for inverted perovskite solar cells. *Nature* **632**, 536–542 (2024).
2. Sanchez-Diaz, J. et al. Tin perovskite solar cells with >1300 h of operational stability in N2 through a synergistic chemical engineering approach. *Joule* **6**, 861–883 (2022).
3. Park, S. M. et al. Engineering ligand reactivity enables high-temperature operation of stable perovskite solar cells. *Science* **381**, 209–215 (2023).
4. Zhang, S. et al. Minimizing buried interfacial defects for efficient inverted perovskite solar cells. *Science* **380**, 404–409 (2023).
5. Wang, J. et al. Colloidal zeta potential modulation as a handle to control the crystallization kinetics of tin halide perovskites for photovoltaic applications. *Angew. Chem. Int. Ed.* **136**, e202317794 (2024).
6. Best research-cell efficiency chart. *NREL* https://www.nrel.gov/pv/cell-efficiency.html (2024).
7. Wang, W. et al. High-performance organic photovoltaic cells under indoor lighting enabled by suppressing energetic disorders. *Joule* **7**, 1067–1079 (2023).
8. Li, C. et al. Bipolar pseudohalide ammonium salts bridged perovskite buried interface toward efficient indoor photovoltaics. *Adv. Energy Mater.* **14**, 2401883 (2024).
9. Wang, K. L. et al. Ion–dipole interaction enabling highly efficient $CsPbI_3$ perovskite indoor photovoltaics. *Adv. Mater.* **35**, 2210106 (2023).
10. Li, Y. et al. In situ formation of 2D perovskite seeding for record-efficiency indoor perovskite photovoltaic devices. *Adv. Mater.* **36**, 2306870 (2024).
11. Lu, W. et al. Lanthanide-like contraction enables the fabrication of high-purity selenium films for efficient indoor photovoltaics. *Angew. Chem. Int. Ed.* **64**, e202413429 (2025).
12. Ma, Q. et al. One-step dual-additive passivated wide-bandgap perovskites to realize 44.72%-efficient indoor photovoltaics. *Energ. Environ. Sci.* **17**, 1637–1644 (2024).
13. Correa Guerrero, N., Guo, Z., Shibayama, N., Jena, A. K. & Miyasaka, T. A semitransparent silver–bismuth iodide solar cell with V oc above 0.8 V for indoor photovoltaics. *ACS Appl. Energy Mater.* **6**, 10274–10284 (2023).
14. Al-Anesi, B. et al. Antimony-bismuth alloying: the key to a major boost in the efficiency of lead-free perovskite-inspired photovoltaics. *Small* **19**, 2303575 (2023).
15. Grandhi, G. K. et al. Perovskite-inspired Cu_2AgBiI_6 for mesoscopic indoor photovoltaics under realistic low-light intensity conditions. *Sustain. Energ. Fuels.* **7**, 66–73 (2023).
16. Grandhi, G. K. et al. Enhancing the microstructure of perovskite-inspired Cu-Ag-Bi-I absorber for efficient indoor photovoltaics. *Small* **18**, 2203768 (2022).
17. Yang, L. et al. Performance improvement of dye-sensitized double perovskite solar cells by adding $Ti_3C_2T_x$ MXene. *Chem. Eng. J.* **446**, 136963 (2022).
18. Arivazhagan, V. et al. Indoor light harvesting lead-free 2-aminothiazolium bismuth iodide solar cells. *Sustain. Energ. Fuels.* **6**, 3179–3186 (2022).
19. Cao, J. J. et al. Multifunctional potassium thiocyanate interlayer for eco-friendly tin perovskite indoor and outdoor photovoltaics. *Chem. Eng. J.* **433**, 133832 (2022).
20. Yang, W. F. et al. Nicotinamide-modified PEDOT: PSS for high performance indoor and outdoor tin perovskite photovoltaics. *Sol. RRL* **5**, 2100713 (2021).
21. Yang, W. F. et al. Suppressed oxidation of tin perovskite by Catechin for eco-friendly indoor photovoltaics. *Appl. Phys. Lett.* **118**, 023501 (2021).
22. Turkevych, I. et al. Potential of AgBiI4 rudorffites for indoor photovoltaic energy harvesters in autonomous environmental nanosensors. *Jpn. J. Appl. Phys.* **60**, SCCE06 (2021).
23. Lamminen, N. et al. Triple A-site cation mixing in 2D perovskite-inspired antimony halide absorbers for efficient indoor photovoltaics. *Adv. Energy Mater.* **13**, 2203175 (2022).
24. Singh, A. et al. Panchromatic heterojunction solar cells for Pb-free all-inorganic antimony based perovskite. *Chem. Eng. J.* **419**, 129424 (2021).
25. Peng, Y. et al. Lead-free perovskite-inspired absorbers for indoor photovoltaics. *Adv. Energy Mater.* **11**, 2002761 (2020).
26. Yang, W. F. et al. Tin halide perovskites: progress and challenges. *Adv. Energy Mater.* **10**, 1902584 (2020).
27. Zhang, M. et al. Low-temperature processed solar cells with formamidinium tin halide perovskite/fullerene heterojunctions. *Nano Res.* **9**, 1570–1577 (2016).
28. Konstantakou, M. & Stergiopoulos, T. A critical review on tin halide perovskite solar cells. *J. Mater. Chem. A.* **5**, 11518–11549 (2017).

29. Gao, Z. et al. Adhesion-controlled heterogeneous nucleation of tin halide perovskites for eco-friendly indoor photovoltaics. *Adv. Mater.* **36**, 2403413 (2024).
30. Fang, H. H. et al. Long-lived hot-carrier light emission and large blue shift in formamidinium tin triiodide perovskites. *Nat. Commun.* **9**, 243 (2018).
31. Brongersma, M. L., Halas, N. J. & Nordlander, P. Plasmon-induced hot carrier science and technology. *Nat. Nanotechnol.* **10**, 25–34 (2015).
32. Liu, C. et al. Dynamics and physical process of hot carriers in optoelectronic devices. *Nano Energy* **95**, 106977 (2022).
33. Li, M. et al. Slow hot-carrier cooling in halide perovskites: prospects for hot-carrier solar cells. *Adv. Mater.* **31**, 1802486 (2019).
34. Kahmann, S. & Loi, M. A. Hot carrier solar cells and the potential of perovskites for breaking the Shockley–Queisser limit. *J. Mater. Chem. C.* **7**, 2471–2486 (2019).
35. Lee, Y. H. Beyond the Shockley-Queisser limit: exploring new frontiers in solar energy harvest. *Science* **383**, eado4308 (2024).
36. Kahmann, S., Shao, S. & Loi, M. A. Cooling, scattering, and recombination—the role of the material quality for the physics of tin halide perovskites. *Adv. Funct. Mater.* **29**, 1902963 (2019).
37. Fu, J. et al. Hot carrier cooling mechanisms in halide perovskites. *Nat. Commun.* **8**, 1–9 (2017).
38. Lin, W. et al. Carrier cooling in lead halide perovskites: a perspective on hot carrier solar cells. *ACS Energy Lett.* **9**, 298–307 (2023).
39. Vardeny, Z. & Tauc, J. Hot-carrier thermalization in amorphous silicon. *Phys. Rev. Lett.* **46**, 1223 (1981).
40. Bernardi, M. et al. Ab initio study of hot carriers in the first picosecond after sunlight absorption in silicon. *Phys. Rev. Lett.* **112**, 257402 (2014).
41. Dai, L. et al. Slow carrier relaxation in tin-based perovskite nanocrystals. *Nat. Photonics* **15**, 696–702 (2021).
42. Chen, Y. et al. Multiple exciton generation in tin–lead halide perovskite nanocrystals for photocurrent quantum efficiency enhancement. *Nat. Photonics* **16**, 485–490 (2022).
43. Cui, J. et al. Surface plasmon resonance effect in inverted perovskite solar cells. *Adv. Sci.* **3**, 1500312 (2016).
44. Saliba, M. et al. Plasmonic-induced photon recycling in metal halide perovskite solar cells. *Adv. Funct. Mater.* **25**, 5038–5046 (2015).
45. Biswas, S. et al. Exciton polaron formation and hot-carrier relaxation in rigid Dion–Jacobson-type two-dimensional perovskites. *Nat. Mater.* **23**, 937–943 (2024).
46. Zheng, Y. et al. Towards 26% efficiency in inverted perovskite solar cells via interfacial flipped band bending and suppressed deep-level traps. *Energ. Environ. Sci.* **17**, 1153–1162 (2024).
47. Li, M. et al. Slow cooling and highly efficient extraction of hot carriers in colloidal perovskite nanocrystals. *Nat. Commun.* **8**, 14350 (2017).
48. Yang, J. et al. Acoustic-optical phonon up-conversion and hot-phonon bottleneck in lead-halide perovskites. *Nat. Commun.* **8**, 14120 (2017).
49. Tian, C. et al. Minimizing interfacial energy loss and volatilization of formamidinium via polymer-assisted D–A supramolecular self-assembly interface for inverted perovskite solar cells with 25.78% efficiency. *Adv. Mater.* **36**, 2404797 (2024).
50. Li, G. et al. Pump fluence dependence of ultrafast carrier dynamics in InSb measured by optical pump–terahertz probe spectroscopy. *Appl. Opt.* **57**, 9729–9734 (2018).
51. Khenkin, M. V. et al. Consensus statement for stability assessment and reporting for perovskite photovoltaics based on ISOS procedures. *Nat. Energy* **5**, 35–49 (2020).
52. Du, S. et al. Inhibiting perovskite decomposition by a creeper-inspired strategy enables efficient and stable perovskite solar cells. *Nat. Commun.* **15**, 5223 (2024).
53. Chu, X. et al. Surface in situ reconstruction of inorganic perovskite films enabling long carrier lifetimes and solar cells with 21% efficiency. *Nat. Energy* **8**, 372–380 (2023).
54. Hu, H. et al. Void-free buried interface for scalable processing of pin-based $FAPbI_3$ perovskite solar modules. *Joule* **7**, 1574–1592 (2023).
55. Sandberg, O. J., Tvingstedt, K., Meredith, P. & Armin, A. Theoretical perspective on transient photovoltage and charge extraction techniques. *J. Phys. Chem. C.* **123**, 14261–14271 (2019).
56. Tran, H. N. 17% non-fullerene organic solar cells with annealing-free aqueous MoO_x. *Adv. Sci.* **7**, 2002395 (2020).
57. Krüger, J. et al. Charge transport and back reaction in solid-state dye-sensitized solar cells: a study using intensity-modulated photovoltage and photocurrent spectroscopy. *J. Phys. Chem. B* **107**, 7536–7539 (2003).
58. Wang, Y. et al. Intensity-modulated photocurrent and photovoltage spectroscopy for characterizing charge dynamics in solar cells. *Adv. Energy Mater.* **14**, 2401585 (2024).
59. Liu, T. et al. Cyano-coordinated tin halide perovskites for wearable health monitoring and weak light imaging. *Adv. Mater.* 2400090 (2024).

Acknowledgements

X.M. acknowledges support from the National Natural Science Foundation of China (22179131, 52232003), the National Key R&D Program of China (2024YFB3614300), the Beijing Natural Science Foundation (2262081), the Fundamental Research Funds for the Central Universities, and the University of Chinese Academy of Sciences. H.X. acknowledges support from the National Natural Science Foundation of China (62304029).

Author contributions

H.X. and X.M. conceived the idea and designed the experiments. X.M. directed and supervised the project. J.L. synthesized the additive molecules. H.X. fabricated solar cell devices and conducted characterizations of the devices. E.C. assisted with PL, TRPL, and PLQY measurements. J.W. and J.H. conducted GIWAX measurements. T.L. assisted with Photo-CELIV measurements. X.W. assisted with NMR measurements. M.A. assisted with the energy level alignment analysis. H.X. wrote the original draft. H.X. and X.M. analyzed the data. J.L., C.W., Z.Z., and X.M. contributed to the editing of the manuscript. All authors discussed the results and reviewed the manuscript.

Competing interests

The authors declare no competing interests.

Additional information

Supplementary information The online version contains supplementary material available at https://doi.org/10.1038/s41467-026-68719-3.

Correspondence and requests for materials should be addressed to Jie Li, Chunru Wang or Xiangyue Meng.

Peer review information *Nature Communications* thanks the anonymous reviewer(s) for their contribution to the peer review of this work. A peer review file is available.